

Towards Physically Interpretable World Models: Meaningful Weakly Supervised Representations for Visual Trajectory Prediction

Zhenjiang Mao, Ivan Ruchkin

University of Florida
z.mao@ufl.edu, iruchkin@ece.ufl.edu

Abstract

Deep learning models are increasingly employed for perception, prediction, and control in autonomous systems. Embedding physical knowledge into these models is crucial for achieving realistic and consistent outputs. However, integrating physical knowledge into representation learning is difficult due to high-dimensional observation data, such as images, particularly under conditions of incomplete or imprecise state information. To address this, we propose *Physically Interpretable World Models*, a novel architecture that aligns learned latent representations with real-world physical quantities. Our method combines a variational autoencoder with an unknown-parameter dynamical model, enabling the discovery of physically meaningful representations. We employ weak interval-based supervision to eliminate the reliance on ground-truth physical annotations. Experimental results demonstrate that our method improves the quality of learned representations while achieving accurate predictions of future states, advancing the field of representation learning for autonomy.

1 Introduction

Autonomous systems in dynamic environments require robust trajectory prediction for safe and efficient operation. Models like Long Short-Term Memory (LSTM) networks [Yu *et al.*, 2019] effectively capture temporal dependencies from raw data. Physics-informed approaches, such as Physics-Informed Neural Networks (PiNNs) [Cai *et al.*, 2021] and Neural Ordinary Differential Equations (Neural ODEs) [Chen *et al.*, 2018], incorporate physical dynamics, merging data-driven learning with first-principles knowledge. However, real-world systems often lack access to full physical states, relying instead on high-dimensional observations, like images or lidar scans, to infer critical properties such as position or safety. The incomplete knowledge of system dynamics is another challenge for physics-informed methods.

Given these challenges, recent research has shifted focus to predicting *observations* to gain insights into system behavior. Convolutional LSTMs [Shi *et al.*, 2015] predict observation sequences but face limitations from high data di-

mensionality and network complexity. While hidden layers extract features, maintaining global consistency across sequences is challenging and has been noted as a limitation in tasks requiring temporal coherence [Shi *et al.*, 2015; Bai *et al.*, 2018]. To address this, many approaches focus on learning *latent representations* to reduce dimensionality and extract relevant features. Variational Autoencoders (VAEs) [Kingma, 2013] are particularly effective, providing unsupervised learning of compact latent spaces and reconstructing high-dimensional data. World models [Ha and Schmidhuber, 2018] extend VAEs by integrating predictive components like mixed-density Recurrent Neural Networks (RNNs) to capture temporal dependencies, enabling accurate action predictions for safety-critical applications [Mao *et al.*, 2024b]. Recent advancements [Micheli *et al.*, 2022] further enhance predictive and generative performance in uncertain environments by combining these structures.

Despite these advantages, the representations learned by these models are merely abstract numbers with limited physical meaning, making it difficult to relate them directly to true internal states. Bridging this gap would improve the interpretability and trustworthiness of predictions and enhance the controllability of autonomous systems in complex, high-risk scenarios. For instance, in autonomous driving, linking latent representations to physical states could generate causal explanations for decisions (e.g., slowing down due to occlusions) and enable high-assurance methods like formal verification [Hasan and Tahar, 2015] and run-time shielding [Waga *et al.*, 2022]. Causal VAEs [Yang *et al.*, 2021] offer a promising solution by learning both meaningful representations and causal relationships, providing structured insights into system dynamics. However, causal VAEs rely heavily on exact supervision labels, which are often challenging to obtain due to constraints on budget, time, and expertise.

This paper addresses trajectory prediction without *exact supervision of physical labels*, by relying on weak supervisory signals to guide representations toward physical meaning. These often overlooked signals can encode valuable constraints, such as a car’s speed rarely exceeding 350 km/h. We represent such constraints as intervals and use them as weak supervision to encode high-dimensional images into physically interpretable representations. Once these representations gain physical meaning, they combine with a learned dynamical system to predict future states, enabling robust

and interpretable decision-making in complex systems.

The goal of this paper is to design *Physically Interpretable World Models* (PIWMs) by embedding dynamics into the prediction pipeline and applying weak supervision to physical states. Using dynamical equations as structural guidance and weak supervision on latent representations, we hypothesize that PIWMs improve the alignment of representations with true physical states. Our research answers two questions: (1) How effectively can weak supervision enable the learning of physically meaningful representations? (2) To what extent can these representations predict future physical states?

Through case studies on the cart pole and lunar lander, we show that our model learns representations closely aligned with physical states and excels in forward prediction tasks. This demonstrates that integrating dynamics and weak supervision improves both interpretability and predictive accuracy.

Our key contributions are:

- A novel architecture for encoding physically meaningful representations in closed-loop systems.
- A training pipeline that integrates weak supervision and adapts to unknown dynamics.
- Experimental results highlighting superior interpretability and accuracy compared to traditional models.

The next section reviews related work. Section 3 details the problem formulation. Section 4 describes our proposed architecture and methodology. Section 5 presents the case study results, and Section 6 concludes the paper.

2 Related Work

2.1 Learning Latent Representations

Latent representations enable neural networks to capture the structure of complex data by encoding it into lower-dimensional spaces. This dimensionality reduction helps models distill key features from high-dimensional data like images, text, and audio while discarding redundant information. Effective latent representations have proven useful in tasks such as image generation [Goodfellow *et al.*, 2020], clustering [Xie *et al.*, 2016], anomaly detection [Mao *et al.*, 2024a], and style transfer [Gatys *et al.*, 2016]. Variational Autoencoders (VAEs) [Kingma, 2013] are commonly used for this purpose, with an encoder compressing input data into a compact latent space and a decoder reconstructing the input. However, standard VAEs fail to enforce interpretable or structured features in the latent space, limiting their suitability for tasks requiring physical meaning.

To improve interpretability, β -VAE [Higgins *et al.*, 2017] introduces a hyperparameter β to disentangle latent features, encouraging independent dimensions in the latent space. While β -VAE provides more structured representations, its features often lack direct correspondence to real-world physical states. Other approaches, such as neural state variables [Chen *et al.*, 2022], employ geometric manifold learning (e.g., the Levina-Bickel algorithm) to ensure latent variables align with physical complexity. CausalVAE enhances interpretability by enforcing causal relationships in the latent space using a causal graph, but these methods rely on labeled causal states, which are difficult to obtain. By contrast, our

approach leverages weak supervision to guide the learning of physically meaningful representations, addressing the challenge of limited labeled data. Task-related domain rules have also been integrated into Bayesian neural networks (e.g., banana [Sam *et al.*, 2024]) to enhance model performance, reliability, and uncertainty quantification. Building on these ideas, we incorporate task-relevant constraints as weak supervision to prioritize physical interpretability and predictive accuracy.

Abstraction techniques further distill high-dimensional data into simplified forms [Fu *et al.*, 2021], highlighting essential motion information while excluding redundant visual details [Wen *et al.*, 2023]. These methods support efficient policy learning but often require supervised labels [Konidaris *et al.*, 2018] or subjective guidance, such as human language [Peng *et al.*, 2024]. Despite their effectiveness, abstraction-based representations are challenging to map back to the original data, limiting their applicability in tasks requiring interoperability.

2.2 Dynamics-Based Learning

In planning and decision-making, world models learn the dynamics of observations under different actions with neural networks, as in Dreamer [Hafner *et al.*, 2020]. These models create simulated environments for policy learning without real-world trials but often lack interpretable latent representations and depend heavily on training data quality and quantity. Their performance degrades when encountering out-of-distribution data due to limited generalization.

To improve the alignment with physical reality, researchers have incorporated constraints on control inputs, such as acceleration and steering, to respect system limits [Tumu *et al.*, 2023]. Embedding motion equations, like kinematic layers [Cui *et al.*, 2020], enables trajectory prediction while adhering to physics. However, these methods require accurate physical data and are prone to errors with noisy or incomplete inputs. Other approaches use constraints such as temporal logic [Ma *et al.*, 2020] or social pooling [Alahi *et al.*, 2016] to shape predictions in low-dimensional scenarios. However, their interpretability diminishes in complex systems, where high-dimensional data and intricate observations make it harder to link latent representations to physical states.

Value-based constraints confine outputs within ranges specified by physical laws [Sridhar *et al.*, 2023], while some methods use physical knowledge as loss functions during training [Djeumou *et al.*, 2023]. Although effective for low-dimensional states, these approaches struggle in high-dimensional settings with partial or noisy sensor data. Physics-informed VAEs [Zhong and Meidani, 2023] and generative ODEs [Linial *et al.*, 2021] leverage the knowledge of differential equations to stabilize learning under physical uncertainty, whereas the Phy-Taylor framework [Mao *et al.*, 2025] uses Taylor monomials. Unfortunately, these approaches still face challenges in the interpretability of representations for high-dimensional inputs like images.

Our approach also incorporates physical dynamics into its architecture — but differs by using weak supervision signals, represented as real-valued intervals, to guide learning without relying on precise physical labels.

2.3 Trajectory Prediction

Predicting trajectories is critical for anticipating hazards like vehicle collisions, providing essential insights for planning and control [Fridovich-Keil *et al.*, 2020]. Traditional methods such as Kalman filtering and Hamilton-Jacobi (HJ) reachability [Li *et al.*, 2021; Nakamura and Bansal, 2023] offer safety guarantees but rely on explicit dynamical models, requiring detailed knowledge of system dynamics and significant computational resources, limiting their applicability in high-dimensional environments.

Deep learning enables flexible trajectory prediction. World models combine autoencoders and recurrent modules to simulate physical scenarios and predict trajectories directly from images [Micheli *et al.*, 2022]. Advanced methods like Trajectron++ [Salzmann *et al.*, 2020] integrate scene graphs with conditional VAEs for multi-agent trajectory forecasting, though they still depend on handcrafted scene representations. Confidence-aware methods [Ruchkin *et al.*, 2022] and conformal prediction [Lindemann *et al.*, 2023] enhance reliability but are orthogonal to physical interpretability. Goal-based Neural Variational Agent (GNeVA) [Lu *et al.*, 2024] models spatial goal distributions using learnable priors, eliminating handcrafted inputs while achieving robust predictions. Interpretable frameworks like ISAP [Itkina and Kochenderfer, 2023] incorporate semantic components such as historical trajectories and high-precision maps, leveraging human-like responsibility metrics [Hsu *et al.*, 2023] to guide predictions aligned with human values.

In contrast, our approach eliminates the need for handcrafted representations, learning directly from images with interval-based weak supervision to achieve interpretable and physically meaningful trajectory predictions.

3 Background and Problem Formulation

3.1 Dynamical System and Sequence Prediction

Definition 1 (Dynamical System). *A dynamical system $s = (X, I, A, \phi_\psi, g, Y)$ describes the state evolution of an image-controller system with any image-based controller h :*

- *State set X : finite-dimensional and containing states x*
- *Initial state set $I \subset X$ and action set A*
- *Dynamics ϕ (with parameters ψ): $X \times A \times \Psi \rightarrow X$*
- *Observation function $g : X \rightarrow Y$*
- *Controller $h : Y \rightarrow A$*

The states of the system evolve as $x_{t+1} = \phi(x_t, a_t, \psi^*)$, where ψ^* are the true physical parameters. The control of such systems usually relies on observations y from sensors. We assume that the controller h is known, as we are observing the controlled system. These controllers are usually trained by imitation learning [Hussein *et al.*, 2017] or reinforcement learning [Kaelbling *et al.*, 1996] like deep deterministic policy gradient (DDPG) [Lillicrap, 2015].

Given an initial state $x_0 \in I$ and a sequence of actions $a_{0:i}$, a *state trajectory* is defined by iteratively applying the dynamics function ϕ , yielding a sequence $(x_0, x_1, \dots, x_{i+1})$, where each state is $x_{t+1} = \phi(x_t, a_t, \psi^*)$. Correspondingly, an *observation trajectory* $(y_0, y_1, \dots, y_{t+1})$ is generated by

applying the observation function g to each state, where $y_t = g(x_t)$. Forecasting observations enables autonomous systems to anticipate potential hazards and adjust their controllers or policies for safe operation, often leveraging computer vision tasks like object detection or semantic segmentation.

Definition 2 (Observation Prediction). *A sequence predictor f_{obs} at time t takes a sequence $y_{t-m:t}$ of m images as input and outputs images $\hat{y}_{t+1:t+n}$ for the next n time steps, represented as the prediction vector $\hat{y}_{(t+1:t+n)} = f_{obs}(y_{t-m:t})$.*

High-quality predictions are essential for downstream tasks, motivating the use of dimensionality-reducing methods to predict *latent representations* when discriminative models like convolutional neural networks (CNNs) struggle with high-dimensional image data. High-dimensional observations require reconstruction for action generation and state prediction, which a VAE achieves by using a CNN-based encoder and a deconvolutional decoder to restore latent representations into task-suitable image forms.

Definition 3 (Latent Sequence Prediction). *An encoder \mathcal{E} compresses the high-dimensional observation input y into a latent representation z and a predictor f_{lat} predicts the future latent representations. A decoder \mathcal{D} to transform the latent representation back to the observation space:*

- *Encoding: $z_{t-m:t} = \mathcal{E}(y_{t-m:t})$*
- *Prediction: $z_{t+1:t+n} = f_{lat}(z_{t-m:t})$*
- *Decoding $\hat{y}_{t+1:t+n} = \mathcal{D}(z_{t+1:t+n})$*

Our primary use case is predicting the behavior of a learning-enabled system, which depends on actions taken by the controller. When the predictor does not explicitly use actions, it implicitly learns the control choices from the training data. This approach limits the model’s generalizability by tying it to a specific controller. To generalize across different controllers, we include the action as additional input alongside the observation or latent representation.

$$y_{t+1} = f_{obs}(y_t, a_t) \text{ or } z_{t+1} = f_{lat}(z_t, a_t) \quad (1)$$

3.2 Physical Representation Learning and Prediction with Weak Supervision

Our setting assumes that the dynamics function of the system ϕ is known in its general form, such as the structure of kinematic equations. However, we do not have access to the true parameters ψ , such as the exact mass or traction coefficients, which makes the system only partially specified. Although true physical states cannot be measured precisely, it is often possible to obtain their reasonable range (e.g., based on a probability distribution) on high-dimensional observations. For instance, the position may be inferred from imprecise image observations or estimated within a predefined range, which can serve as a weak supervisory signal.

We are also given a dataset \mathcal{S} of trajectories, consisting of N sequences of length M , where each sequence contains tuples of images, actions, and state interval labels:

$$\mathcal{S} = \left\{ (y_{1:M}, a_{1:M}, [x_{1:M}^{lo}, x_{1:M}^{up}])_{1:N} \right\} \quad (2)$$

The state intervals $[x^{lo}, x^{up}]$ will be used as weak supervision signals. These intervals are typically large, spanning

1–10% of the *entire state space*, indicating highly imprecise information about the states. The representation learning problem is to obtain an internal representation z that approximates the system’s true physical states x . To evaluate the physicality of this representation, we use the mean absolute error MAE metric. Given a sample initial observation y from the test dataset \mathcal{S}' , we compute the corresponding interpretable latent z .

Definition 4 (Representation Learning Problem). *Given training dataset \mathcal{S} , and controller h , the objective is to learn a state representation $z = \mathcal{E}(y)$ that minimizes the distance to the true physical state x :*

$$\min_{\mathcal{E}} \|x - \mathcal{E}(y)\|_1 \quad (3)$$

The prediction problem aims to forecast future observations and state representations using past observations, actions, and constraints. We formulate it to emphasize the role of latent physically interpretable representations.

Definition 5 (Prediction Problem with Meaningful Representation). *Given a training dataset \mathcal{S} , dynamics function ϕ with unknown parameters, and controller h , the objective is to train predictors for the future observation y_{t+k} and the future physical state representation z_{t+k} at time $t + k$ from current observation y_t by minimizing two errors:*

1. *Observation prediction error:*

$$\min \|y_{t+k} - \hat{y}_{t+k}\|_2^2 \quad (4)$$

2. *State prediction error:*

$$\min \|x_{t+k} - z_{t+k}\|_1, \quad (5)$$

where \hat{y}_{t+k}^i is the predicted observation at time $t+k$ predicted from the i -th sequence of the dataset \mathcal{S} , y_{t+k}^i is the true observation, and z_{t+k}^i is the predicted state representation aligned with the true physical state x_{t+k}^i .

To comprehensively evaluate the quality of the predicted observations, we use both Mean Squared Error (MSE) and Structural Similarity Index (SSIM) metrics. MSE measures the average pixel-wise error, offering a straightforward quantitative assessment of overall accuracy. However, it does not account for perceptual quality or structural integrity, which are crucial for visual consistency. SSIM, on the other hand, captures structural similarity by considering luminance, contrast, and covariance, making it more similar to human perception of image quality. By combining these metrics, we ensure both numerical accuracy and perceptual fidelity in evaluating the alignment between the predicted and the true ones.

4 Physically Interpretable World Models

Our *physically interpretable world models* (PIWMs) use a standard VAE structure as a skeleton. The encoder \mathcal{E} takes the observation y_t as input and the output z_t has the same dimension as the state x_t . A customized dynamical layer ϕ is designed as a sequence predictor to generate predicted state z_{t+1} at the next moment. Finally, the decoder \mathcal{D} takes the latent representation z_{t+1} as input to reconstruct the image \hat{y}_{t+1} . This reconstructed observation serves as the predicted

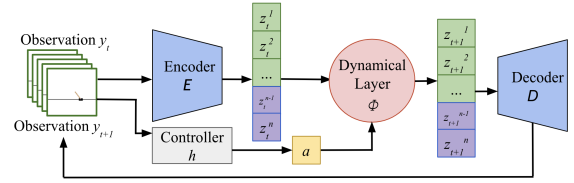


Figure 1: Our architecture for physically interpretable world models. The green latent representations z approximate physical states.

observation for the next moment and is specifically designed as input to the controller to generate an action a_{t+1} . The generated action a_{t+1} is applied to the environment to influence the system’s next state, closing the feedback loop. Fig. 1 shows the overview of our proposed architecture:

1. **Encoder** converts observations into physically meaningful latent representations (Section 4.2).
2. **Dynamical Layer** predicts the next latent vector based on the current one and the action (Section 4.1).
3. **Decoder** reconstructs the observation from the predicted latent vector and feeds it into the controller (Section 4.2).

The loss function of PIWM combines the reconstruction loss and the weakly-supervised physical signal. The main challenge in implementing PIWM is giving the latent values a physical meaning while maintaining efficient encoding and high-performance decoding under weak supervision.

4.1 Dynamical Layer for Temporal Prediction

Since the system’s dynamics function ϕ operates in a lower-dimensional space, we introduce a latent representation z , and $\dim(z) \geq \dim(x)$. The first $\dim(x)$ dimensions of the latent representation $z' = z[0 : \dim(x)]$ are assigned to represent the physical states corresponding to x , ensuring consistency between the latent space and the original state space. The other, non-physical dimensions $z^* = z[\dim(x) + 1 : \dim(z)]$ are intended for other distributed features useful to image decoding. The latent representation z' serves as the input to the dynamics function, allowing the model to predict the future latent state. Non-physical state variables will remain constant as the first encoded representations. Mathematically, this is expressed as:

$$z'_{t+1} = \phi(z'_t, a_t, \psi) \quad (6)$$

This dynamics function forms the core of the *dynamical layer*, a prediction module integrated into our model architecture. While the structure of the dynamics function (i.e., its governing equations) is known, the exact values of its true parameters, denoted as ψ^* , are unknown. The parameters ψ within this layer are learnable and initialized randomly, enabling the model to approximate ψ^* during training (details in Section 4.3). For example, in a cart-pole system, the state x includes variables such as the cart’s position, velocity, and the pole’s angle and angular velocity. By encoding the observation y into latent dimensions z' , the model captures the physical relationships among these variables, allowing for an interpretable and physically consistent evolution.

4.2 Encoding/Decoding Physically Interpretable Representations with Weak Supervision

Variational Inference: Our model’s encoder and decoder structures are based on the VAE framework [Kingma, 2013], where observed data y is generated from a latent variable z via $p(y | z)$, to learn a compact z that captures essential features by maximizing the marginal likelihood $p(y)$. However, directly computing $p(y)$ is generally intractable due to the complexity of integrating over z . To address this, VAE introduces an approximate posterior distribution $q(z|y)$, which represents the probability of latent z given the data y . This approximation is parameterized by the encoder network \mathcal{E} and serves as a tractable substitute for the true posterior $p(z|y)$. This approximation step is also the basis for our approach of approximating the uncertain physical values (e.g., the positions and angles) implied by an image observation.

In standard VAEs, the latent variable z is typically constrained by a standard Gaussian prior distribution $p(z) = \mathcal{N}(0, 1)$, to regularize the latent space. This technique helps avoid discontinuities and poor-performance “holes” in the latent space around value 0. Unfortunately, it results in z being an abstract, non-physical representation with values around 0. **Incorporating Weak Supervision:** In our approach, we change that prior by incorporating weak supervisory signals to make z more physically meaningful. To achieve this, we utilize available interval constraints from the training data \mathcal{S} , which capture physical ranges or limits. To stay compatible with the Gaussian-based KL divergence used in VAE training, we encode the intervals as Gaussian distributions centered within the intervals. By aligning the latent representation z' with these distributions, our PIWM makes z' reflect the physical properties of the system, not necessarily close to 0.

Specifically, VAEs are trained by maximizing a lower bound on $\log p(y)$, a.k.a. the evidence lower bound (ELBO):

$$\log p(y) \geq \mathbb{E}_{q(z|y)} [\log p(y|z)] - D_{KL}(q(z|y) \parallel \mathcal{N}(0, 1)),$$

where the first term, $\mathbb{E}_{q(z|y)} [\log p(y|z)]$, represents the expected log-likelihood of the data y given a latent z . This term quantifies how well the decoder, which generates y from z , reconstructs the input data and is thus related to the reconstruction accuracy. The second term, $D_{KL}(q(z|y) \parallel \mathcal{N}(0, 1))$, is the Kullback-Leibler (KL) divergence from the normal prior.

We extend the ELBO objective function below to regularize the latent space with the weakly supervised intervals:

$$\log p(y) \geq \mathbb{E}_{q(z|y)} [\log p(y|z)] - D_{KL}(q(z|y) \parallel \mathcal{N}(\mu', \sigma'^2)),$$

where $\mathcal{N}(\mu', \sigma'^2)$ replaces the prior distribution $\mathcal{N}(0, 1)$ and represents the Gaussian fit to the weak supervision signal. The mean μ' is set to the center of the given interval, $\mu_p^i = \frac{x_{lo}^i + x_{up}^i}{2}$, and the standard deviation σ' is defined as $\sigma_p^i = \frac{x_{up}^i - x_{lo}^i}{6}$, such that the interval aligns with the $\pm 3\sigma$ range of a Gaussian distribution, covering approximately 99.73% of the probability mass. Thus, the KL divergence term encourages z to align with physical ranges, ensuring that the latent space is organized around real physical value ranges rather than an arbitrary standard normal prior. For non-physical dimensions z^* , $\mathcal{N}(0, 1)$ is applied as a prior.

Our learned representation z also uses the reparameterization trick common in VAEs, which allows for gradient-based optimization while preserving the model’s stochastic nature. Specifically, the latent variable z is computed as:

$$z = f_{enc}(y) = \mu(y) + \sigma(y) \cdot \epsilon, \quad (7)$$

where $\epsilon \sim \mathcal{N}(0, I)$ is standard Gaussian noise, and $\mu(y)$ and $\sigma(y)$ are the outputs from two heads of the encoder.

Observation and State Predictions: The decoder’s output forms our predicted observation:

$$\hat{y} = \mathcal{D}(z) \quad (8)$$

The target latent distribution $p(z_{t+1})$ is modeled as a multi-variate Gaussian due to the multi-dimensionality of the states:

$$p(z_{t+1}) = \mathcal{N}(z_{t+1}; \mu_p, \text{diag}((\sigma_p^i)^2)), \quad (9)$$

where $\mu_p = [\mu_p^1, \mu_p^2, \dots, \mu_p^d]$ and $\text{diag}((\sigma_p^i)^2)$ is the diagonal covariance matrix with entries $(\sigma_p^1)^2, (\sigma_p^2)^2, \dots, (\sigma_p^d)^2$, each corresponding to one of the d dimensions of z .

4.3 Training for Physical Interpretability

Loss Function: To further align representations with physical reality, we extract the knowledge in a controller to penalize large changes in images. In particular, suppose $h(y)$ and $h(y_{recon})$ are the controller actions on the real image and reconstructed image. $h(y_{recon})_{h(y)}$ denotes the probability value assigned by the distribution $h(y_{recon})$ to the true action class $h(y)$. Their difference is computed with a cross-entropy term \mathcal{L}_{CE} . Thus, the PIWM loss function incorporates image reconstruction, dynamical prediction with weak supervision, and controller penalty:

$$\begin{aligned} \mathcal{L} &= -\mathbb{E}_{q(z|y)} [\log p(y|z)] + \lambda_1 D_{KL}(q(z_{t+1}|z_t) \parallel p(z_{t+1})) \\ &\quad + \lambda_2 \mathcal{L}_{CE}(h(y), h(y_{recon})) \\ &= -\mathbb{E}_{q(z|y)} [\log p(y|z)] + \lambda_1 \sum_z q(z_{t+1}|z_t) \log \frac{q(z_{t+1}|z_t)}{p(z_{t+1})} \\ &\quad - \lambda_2 \cdot \log(h(y_{recon})_{h(y)}) \end{aligned}$$

Our approach learns the unknown parameters ψ within the dynamical layer and the parameters of the encoder-decoder pair, aligning the latent space with representations that are consistent with the system’s physical dynamics and making use of weak supervision to capture meaningful physical states across each dimension.

Efficient Training via Amortized Inference: As mentioned, our key challenge is to efficiently learn latent representations that are both physically grounded and capable of generalizing across diverse physical ranges defined by weak supervision. To address it, we adopt *amortized variational inference* [Gershman and Goodman, 2014], where the encoder neural network shares parameters across all data points rather than optimizing separate variational parameters for each instance. By doing so, the encoder leverages common structural patterns within the dataset, ensuring that the learned latent representations z remain coherent and physically meaningful. This parameter sharing not only reduces computational overhead but

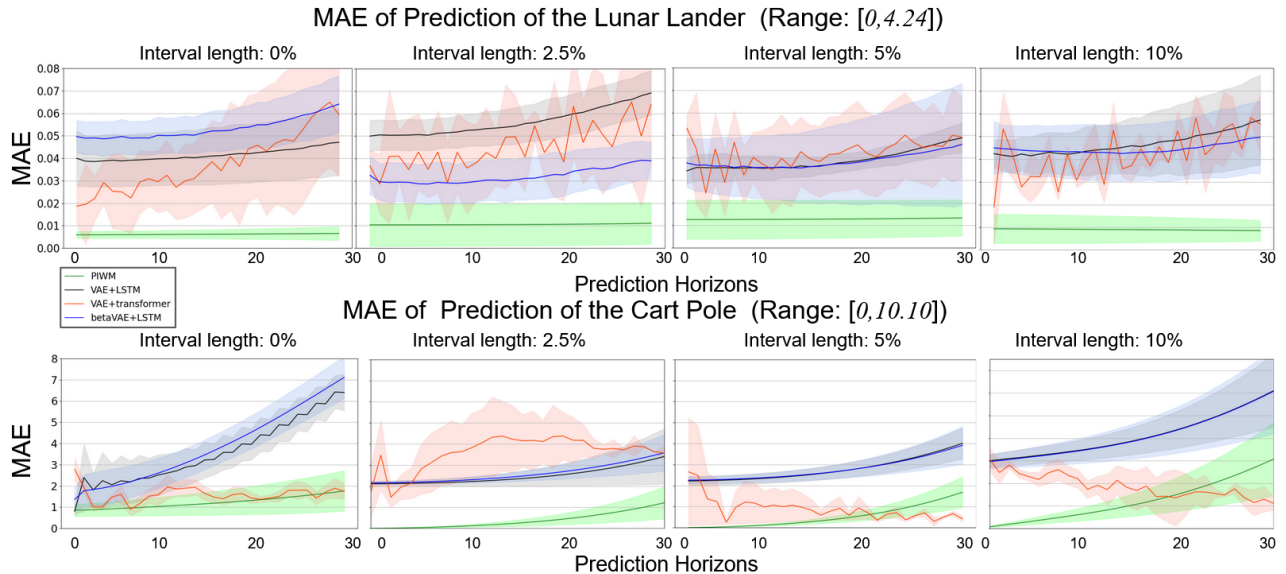


Figure 2: Results of the MAE of prediction: lunar lander (upper) and cartpole (lower). Shaded areas indicate uncertainty.

also facilitates scaling to larger datasets, resulting in a more robust inference process for varied physical scenarios.

Gradients: The loss function \mathcal{L} which represents the objective for optimizing the system’s performance during training, which could evaluate the final state x_T (e.g., the error between the predicted and true state, or other metrics such as energy efficiency or safety violations) or depend on the entire trajectory $\{x_1, \dots, x_T\}$ (e.g., cumulative errors or rewards over time).

The gradient of \mathcal{L} with respect to ψ , which governs the dynamics $\phi(x, a, \psi)$, can be expressed as:

$$\frac{\partial \mathcal{L}}{\partial \psi} = \frac{\partial \mathcal{L}}{\partial x_T} \cdot \frac{\partial x_T}{\partial \psi}. \quad (10)$$

Here, $\frac{\partial \mathcal{L}}{\partial x_T}$ measures how the loss changes with the final state, while $\frac{\partial x_T}{\partial \psi}$ captures the sensitivity of the state dynamics to the parameters ψ . This formulation directly relates to the loss function used in training, allowing the model to optimize the dynamics parameters ψ via gradient-based backpropagation to achieve task-specific objectives.

Since x_T depends on the states in previous time steps and parameters ψ , we can expand this as:

$$\frac{\partial x_T}{\partial \psi} = \frac{\partial \phi(x_{T-1}, a_{T-1}, \psi)}{\partial \psi} + \frac{\partial \phi(x_{T-1}, a_{T-1}, \psi)}{\partial x_{T-1}} \cdot \frac{\partial x_{T-1}}{\partial \psi}$$

This formula expresses the second gradient of Equation 10 in terms of a gradient of ϕ_ψ with respect to its parameters, a Jacobian matrix $\frac{\partial \phi(x_{T-1}, a_{T-1}, \psi)}{\partial x_{T-1}}$, and the same gradient for the previous state.

By recursively applying this formula, we compute gradients over the prediction horizon of k steps. The entire training procedure is detailed in the appendix in Algorithm 1, which describes the process of jointly learning physical representation and dynamics with batch input.

5 Experimental Evaluation

Our experiments evaluate the accuracy of PIWM trajectory prediction on two simulated environments from OpenAI’s gym [Brockman *et al.*, 2016]: the cartpole and lunar lander. To check for learning the physical knowledge, we examine the alignment of learned dynamics parameters with the true ones. We also perform ablation studies under varying time horizons and levels of noise in the supervision signal, as well as removing the dynamical layer.

We chose the cart pole and lunar lander because they differ in complexity and dimensionality. The cart pole task involves balancing a pole on a moving cart with a four-dimensional state space and a binary action space, while the lunar lander task requires guiding a lander to a safe landing with an eight-dimensional state space and a four-dimensional action space. We collected $N = 60,000$ trajectories in each study, with $M = 50$ time steps per trajectory, using controllers trained with the DQN algorithm. As weak supervision, interval constraints of varying lengths (2.5%, 5%, and 10% of the state space) were generated on top of the true state. The interval centers were randomly shifted within their respective ranges, ensuring that the true values remained within the intervals but not necessarily at the center.

5.1 Results

Prediction Accuracy: For the Lunar Lander environment, the PIWM model demonstrates strong performance in predicting the lander’s 2D position, as reflected by its MAE of Euclidean distance error as shown in Figure 2. From 0 to 30 steps, PIWM maintains consistently low prediction errors. In the ablation study comparing VAE+LSTM and β -VAE+LSTM models, the following observations were made: when the interval length is 0, the β -VAE LSTM model performs better than the VAE-based models; at an interval length of 2.5%, the β -VAE model performs worse than the VAE-

Table 1: Evaluation of learned dynamics parameters.

| Types | Parameters of Lunar Lander | | | Parameters of Cart Pole | | |
|-------|----------------------------|------------------------|---------------|-------------------------|---------------|-----------------|
| | $power_{main_engine}$ | $power_{side_engine}$ | $mass_{pole}$ | $length_{pole}$ | $mass_{cart}$ | $force$ |
| True | 13.0 | 0.6 | 0.1 | 0.5 | 1 | 10 |
| 0 | 11.638±0.059 | 0.526±0.011 | 0.424 ± 0.275 | 2.605 ± 0.902 | 5.199 ± 1.656 | 56.857 ± 14.218 |
| 2.5% | 12.174±0.025 | 0.610±0.010 | 0.504 ± 0.180 | 2.129 ± 0.954 | 5.137 ± 2.225 | 57.764 ± 16.671 |
| 5% | 11.981±0.054 | 0.592±0.004 | 0.670 ± 0.181 | 3.181 ± 0.999 | 5.447 ± 1.256 | 45.047 ± 25.429 |
| 10% | 11.357±0.004 | 0.475±0.026 | 0.369 ± 0.094 | 2.189 ± 1.049 | 3.019 ± 1.373 | 49.565 ± 25.397 |

Table 2: Observation prediction results.

| Types | Lunar Lander | | Cart Pole | |
|-------|-----------------|---------------|-----------------|---------------|
| | MSE | SSIM | MSE | SSIM |
| True | 0 | 1 | 0 | 1 |
| 0% | 0.0003 ± 0.0011 | 0.979 ± 0.012 | 0.0002 ± 0.0001 | 0.994 ± 0.004 |
| 2.5% | 0.0008 ± 0.0010 | 0.972 ± 0.009 | 0.0003 ± 0.0001 | 0.977 ± 0.012 |
| 5% | 0.0004 ± 0.0008 | 0.980 ± 0.015 | 0.0009 ± 0.0014 | 0.965 ± 0.038 |
| 10% | 0.0009 ± 0.0015 | 0.980 ± 0.011 | 0.0003 ± 0.0001 | 0.969 ± 0.014 |

based models; and at interval lengths of 5% and 10%, both models perform similarly. Additionally, the Transformer model exhibits higher variability in its predictions. For interval lengths of 0% and 2.5%, the Transformer’s performance lies between the VAE and β -VAE LSTM models, while for interval lengths of 5% and 10%, it performs similarly to LSTM-based models without attention mechanisms. Overall, LSTM and Transformer models, which are purely data-driven and rely solely on historical trajectories, fail to match the predictive accuracy of the proposed PIWM model. By incorporating dynamics parameter learning and leveraging these parameters for predictions, PIWM demonstrates superior accuracy and stability. Additionally, it is worth noting that PIWM exhibits balanced performance in predicting both the horizontal and vertical positions, maintaining consistently low error levels across both dimensions. In contrast, the other three ablation models demonstrate imbalanced prediction behavior, as shown in the additional results presented in the Appendix. For instance, in the 2.5% interval VAE LSTM model, the horizontal position prediction performs comparably to PIWM for the first 0–15 steps, but the vertical position prediction suffers from significantly higher errors.

For the Cart Pole environment, we evaluated the Euclidean distance and computed the MAE for the cart’s position and the pole’s angle. Our proposed dynamics-based PIWM consistently outperforms all other models within the 0–20 step range. Between 20–30 steps, the Transformer model exhibits smaller prediction errors but remains highly unstable, with errors over steps being less smooth. Meanwhile, the results of the β -VAE LSTM and VAE LSTM models become very similar, indicating that the β -VAE does not contribute to improving the feature distribution in the latent space. Additionally, the errors increase as the weak supervision signal becomes less precise as the interval length grows.

In both environments, PIWMs demonstrate the balancing of prediction accuracy and physical interpretability and achieve superior results under varying complexity.

Dynamics Parameters and Observation Prediction: One way to determine whether the pipeline is learning physical

knowledge is to compare its learned dynamics parameters (which receive no supervision) to their true values. For the lunar lander, the PIWM model demonstrates strong performance in learning dynamic parameters as shown in Table 1. Even as the supervision signals weaken, the learned parameters remain highly accurate and closely approximate the true values. This robustness underscores the model’s ability to capture essential physical information under varying levels of weak supervision.

For the cartpole environment, the learned parameters exhibit a surprising invariant property: all parameters are scaled approximately five times larger than their true values. This reflects a typical issue in dynamical systems where multiple sets of parameters can lead to nearly identical trajectories. Specifically, if both the cart and pole masses, as well as the applied force, are increased by the same factor, the resulting acceleration remains unchanged, leading to the same trajectory. This observation highlights potential ambiguity in parameter identification and suggests future work in this direction.

Overall, the PIWM model effectively learns dynamic parameters in both environments, balancing prediction accuracy and interpretability even under challenging conditions. Additionally, both the MSE and SSIM metrics are within excellent, reasonable ranges, ensuring that the model effectively reconstructs observations consistent with the underlying dynamics as shown in Table 2.

6 Conclusion

In summary, PIWM provides a reliable framework for encoding physically meaningful representations and achieving accurate predictions, advancing the development of interpretable world models for autonomous systems.

Our PIWM model excels in both short-term and long-term prediction tasks, consistently outperforming baselines in the simulated experiments under weak supervision. It effectively aligns learned representations with true physical states, making it suitable for applications with partial state information and limited labeled data.

Future enhancements of PIWMs include incorporating finer-grained physical constraints, adaptive supervision, and varying learning rates for long prediction horizons. Additionally, leveraging invariances in physical systems — such as symmetries in motion dynamics or conservation laws — could further improve the model’s robustness and generalizability. Such enhancements would broaden PIWM’s applicability across diverse physical systems with varying levels of observability and supervision.

While prediction accuracy declines slightly with weaker supervision or longer prediction horizons, PIWM remains interpretable in high-dimensional tasks. Future work could incorporate adaptive supervision or leverage physical invariances to enhance robustness and broaden applicability to diverse physical systems.

References

- [Alahi *et al.*, 2016] Alexandre Alahi, Kratharth Goel, Vignesh Ramanathan, Alexandre Robicquet, Li Fei-Fei, and Silvio Savarese. Social lstm: Human trajectory prediction in crowded spaces. In *Proc. of the IEEE conference on computer vision and pattern recognition*, 2016.
- [Bai *et al.*, 2018] Shaojie Bai, J Zico Kolter, and Vladlen Koltun. An empirical evaluation of generic convolutional and recurrent networks for sequence modeling. *arXiv preprint arXiv:1803.01271*, 2018.
- [Brockman *et al.*, 2016] Greg Brockman, Vicki Cheung, Ludwig Pettersson, Jonas Schneider, John Schulman, Jie Tang, and Wojciech Zaremba. Openai gym, 2016.
- [Cai *et al.*, 2021] Shengze Cai, Zhiping Mao, Zhicheng Wang, Minglang Yin, and George Em Karniadakis. Physics-informed neural networks (pinns) for fluid mechanics: A review. *Acta Mechanica Sinica*, 37(12):1727–1738, 2021.
- [Chen *et al.*, 2018] Ricky TQ Chen, Yulia Rubanova, Jesse Bettencourt, and David K Duvenaud. Neural ordinary differential equations. *Advances in neural information processing systems*, 31, 2018.
- [Chen *et al.*, 2022] Boyuan Chen, Kuang Huang, Sunand Raghupathi, Ishaan Chandratreya, Qiang Du, and Hod Lipson. Automated discovery of fundamental variables hidden in experimental data. *Nature Computational Science*, 2(7):433–442, 2022.
- [Cui *et al.*, 2020] Henggang Cui, Thi Nguyen, Fang-Chieh Chou, Tsung-Han Lin, Jeff Schneider, David Bradley, and Nemanja Djuric. Deep kinematic models for kinematically feasible vehicle trajectory predictions. In *2020 IEEE International Conference on Robotics and Automation (ICRA)*, pages 10563–10569. IEEE, 2020.
- [Djeumou *et al.*, 2023] Franck Djeumou, Cyrus Neary, and Ufuk Topcu. How to learn and generalize from three minutes of data: Physics-constrained and uncertainty-aware neural stochastic differential equations. *arXiv preprint arXiv:2306.06335*, 2023.
- [Fridovich-Keil *et al.*, 2020] David Fridovich-Keil, Andrea Bajcsy, Jaime F Fisac, Sylvia L Herbert, Steven Wang, Anca D Dragan, and Claire J Tomlin. Confidence-aware motion prediction for real-time collision avoidance1. *The International Journal of Robotics Research*, 39(2-3):250–265, 2020.
- [Fu *et al.*, 2021] Xiang Fu, Ge Yang, Pulkit Agrawal, and Tommi Jaakkola. Learning task informed abstractions. In *International Conference on Machine Learning*, pages 3480–3491. PMLR, 2021.
- [Gatys *et al.*, 2016] Leon A Gatys, Alexander S Ecker, and Matthias Bethge. Image style transfer using convolutional neural networks. In *Proc. of the IEEE conference on computer vision and pattern recognition*, 2016.
- [Gershman and Goodman, 2014] Samuel Gershman and Noah Goodman. Amortized inference in probabilistic reasoning. In *Proceedings of the annual meeting of the cognitive science society*, volume 36, 2014.
- [Goodfellow *et al.*, 2020] Ian Goodfellow, Jean Pouget-Abadie, Mehdi Mirza, Bing Xu, David Warde-Farley, Sherjil Ozair, Aaron Courville, and Yoshua Bengio. Generative adversarial networks. *Communications of the ACM*, 63(11):139–144, 2020.
- [Ha and Schmidhuber, 2018] David Ha and Jürgen Schmidhuber. World models. *arXiv preprint arXiv:1803.10122*, 2018.
- [Hafner *et al.*, 2020] Danijar Hafner, Timothy Lillicrap, Mohammad Norouzi, and Jimmy Ba. Mastering atari with discrete world models. *arXiv preprint arXiv:2010.02193*, 2020.
- [Hasan and Tahar, 2015] Osman Hasan and Sofiene Tahar. Formal verification methods. In *Encyclopedia of Information Science and Technology, Third Edition*, pages 7162–7170. IGI global, 2015.
- [Higgins *et al.*, 2017] Irina Higgins, Loic Matthey, Arka Pal, Christopher P Burgess, Xavier Glorot, Matthew M Botvinick, Shakir Mohamed, and Alexander Lerchner. beta-vaе: Learning basic visual concepts with a constrained variational framework. *ICLR (Poster)*, 3, 2017.
- [Hsu *et al.*, 2023] Kai-Chieh Hsu, Karen Leung, Yuxiao Chen, Jaime F Fisac, and Marco Pavone. Interpretable trajectory prediction for autonomous vehicles via counterfactual responsibility. In *2023 IEEE/RSJ International Conference on Intelligent Robots and Systems (IROS)*, pages 5918–5925. IEEE, 2023.
- [Hussein *et al.*, 2017] Ahmed Hussein, Mohamed Medhat Gaber, Eyad Elyan, and Chrisina Jayne. Imitation learning: A survey of learning methods. *ACM Computing Surveys (CSUR)*, 50(2):1–35, 2017.
- [Itkina and Kochenderfer, 2023] Masha Itkina and Mykel Kochenderfer. Interpretable self-aware neural networks for robust trajectory prediction. In *Conference on Robot Learning*, pages 606–617. PMLR, 2023.
- [Kaelbling *et al.*, 1996] Leslie Pack Kaelbling, Michael L Littman, and Andrew W Moore. Reinforcement learning: A survey. *Journal of artificial intelligence research*, 4:237–285, 1996.
- [Kingma, 2013] Diederik P Kingma. Auto-encoding variational bayes. *arXiv preprint arXiv:1312.6114*, 2013.
- [Konidaris *et al.*, 2018] George Konidaris, Leslie Pack Kaelbling, and Tomas Lozano-Perez. From skills to symbols: Learning symbolic representations for abstract high-level planning. *Journal of Artificial Intelligence Research*, 61:215–289, 2018.

- [Li *et al.*, 2021] Anjian Li, Liting Sun, Wei Zhan, Masayoshi Tomizuka, and Mo Chen. Prediction-based reachability for collision avoidance in autonomous driving. In *2021 Intl. Conf. on Robotics and Automation (ICRA)*, 2021.
- [Lillicrap, 2015] TP Lillicrap. Continuous control with deep reinforcement learning. *arXiv preprint arXiv:1509.02971*, 2015.
- [Lindemann *et al.*, 2023] Lars Lindemann, Xin Qin, Jyotirmoy V Deshmukh, and George J Pappas. Conformal prediction for stl runtime verification. In *Proceedings of the ACM/IEEE 14th International Conference on Cyber-Physical Systems (with CPS-IoT Week 2023)*, pages 142–153, 2023.
- [Linial *et al.*, 2021] Ori Linial, Neta Ravid, Danny Eytan, and Uri Shalit. Generative ODE modeling with known unknowns. In *Proceedings of the Conference on Health, Inference, and Learning, CHIL '21*, pages 79–94, New York, NY, USA, April 2021. Association for Computing Machinery.
- [Lu *et al.*, 2024] Juanwu Lu, Wei Zhan, Masayoshi Tomizuka, and Yeping Hu. Towards generalizable and interpretable motion prediction: A deep variational bayes approach. In *International Conference on Artificial Intelligence and Statistics*, pages 4717–4725. PMLR, 2024.
- [Ma *et al.*, 2020] Meiyi Ma, Ji Gao, Lu Feng, and John Stankovic. Stlnet: Signal temporal logic enforced multivariate recurrent neural networks. *Advances in Neural Information Processing Systems*, 33:14604–14614, 2020.
- [Mao *et al.*, 2024a] Zhenjiang Mao, Dong-You Jhong, Ao Wang, and Ivan Ruchkin. Language-enhanced latent representations for out-of-distribution detection in autonomous driving. *Robot Trust for Symbiotic Societies Workshop at IEEE ICRA*, 2024.
- [Mao *et al.*, 2024b] Zhenjiang Mao, Carson Sobolewski, and Ivan Ruchkin. How safe am i given what i see? calibrated prediction of safety chances for image-controlled autonomy. In *6th Annual Learning for Dynamics & Control Conference*, pages 1370–1387. PMLR, 2024.
- [Mao *et al.*, 2025] Yanbing Mao, Yuliang Gu, Lui Sha, Huajie Shao, Qixin Wang, and Tarek Abdelzaher. Phy-Taylor: Partially Physics-Knowledge-Enhanced Deep Neural Networks via NN Editing. *IEEE Transactions on Neural Networks and Learning Systems*, 36(1):447–461, January 2025.
- [Micheli *et al.*, 2022] Vincent Micheli, Eloi Alonso, and François Fleuret. Transformers are sample-efficient world models. *arXiv preprint arXiv:2209.00588*, 2022.
- [Nakamura and Bansal, 2023] Kensuke Nakamura and Somil Bansal. Online update of safety assurances using confidence-based predictions. In *2023 IEEE International Conference on Robotics and Automation (ICRA)*, pages 12765–12771. IEEE, 2023.
- [Peng *et al.*, 2024] Andi Peng, Mycal Tucker, Eoin Kenny, Noga Zaslavsky, Pulkit Agrawal, and Julie A Shah. Human-guided complexity-controlled abstractions. *Advances in Neural Information Processing Systems*, 36, 2024.
- [Ruchkin *et al.*, 2022] Ivan Ruchkin, Matthew Cleaveland, Radoslav Ivanov, Pengyuan Lu, Taylor Carpenter, Oleg Sokolsky, and Insup Lee. Confidence composition for monitors of verification assumptions. In *2022 ACM/IEEE 13th International Conference on Cyber-Physical Systems (ICCCPS)*, pages 1–12. IEEE, 2022.
- [Salzmann *et al.*, 2020] Tim Salzmann, Boris Ivanovic, Punarjay Chakravarty, and Marco Pavone. Trajectron++: Dynamically-feasible trajectory forecasting with heterogeneous data. In *Computer Vision—ECCV 2020: 16th European Conference, Glasgow, UK, August 23–28, 2020, Proceedings, Part XVIII 16*, pages 683–700. Springer, 2020.
- [Sam *et al.*, 2024] Dylan Sam, Rattana Pukdee, Daniel P Jeong, Yewon Byun, and J Zico Kolter. Bayesian neural networks with domain knowledge priors. *arXiv preprint arXiv:2402.13410*, 2024.
- [Shi *et al.*, 2015] Xingjian Shi, Zhourong Chen, Hao Wang, Dit-Yan Yeung, Wai-Kin Wong, and Wang-chun Woo. Convolutional lstm network: A machine learning approach for precipitation nowcasting. *Advances in neural information processing systems*, 28, 2015.
- [Sridhar *et al.*, 2023] Kaustubh Sridhar, Souradeep Dutta, James Weimer, and Insup Lee. Guaranteed conformance of neurosymbolic models to natural constraints. In *Learning for Dynamics and Control Conference*, pages 76–89. PMLR, 2023.
- [Tumu *et al.*, 2023] Renukanandan Tumu, Lars Lindemann, Truong Nghiem, and Rahul Mangharam. Physics constrained motion prediction with uncertainty quantification. In *2023 IEEE Intelligent Vehicles Symposium (IV)*, pages 1–8. IEEE, 2023.
- [Waga *et al.*, 2022] Masaki Waga, Ezequiel Castellano, Sasi-nee Pruekprasert, Stefan Klikovits, Toru Takisaka, and Ichiro Hasuo. Dynamic shielding for reinforcement learning in black-box environments. In *International Symposium on Automated Technology for Verification and Analysis*, pages 25–41. Springer, 2022.
- [Wen *et al.*, 2023] Chuan Wen, Xingyu Lin, John So, Kai Chen, Qi Dou, Yang Gao, and Pieter Abbeel. Any-point trajectory modeling for policy learning. *arXiv preprint arXiv:2401.00025*, 2023.
- [Xie *et al.*, 2016] Junyuan Xie, Ross Girshick, and Ali Farhadi. Unsupervised deep embedding for clustering analysis. In *International conference on machine learning*, pages 478–487. PMLR, 2016.
- [Yang *et al.*, 2021] Mengyue Yang, Furui Liu, Zhitang Chen, Xinwei Shen, Jianye Hao, and Jun Wang. Causalvae: Disentangled representation learning via neural structural causal models. In *Proceedings of the IEEE/CVF conference on computer vision and pattern recognition*, pages 9593–9602, 2021.

[Yu *et al.*, 2019] Yong Yu, Xiaosheng Si, Changhua Hu, and Jianxun Zhang. A review of recurrent neural networks: Lstm cells and network architectures. *Neural computation*, 31(7):1235–1270, 2019.

[Zhong and Meidani, 2023] Weiheng Zhong and Hadi Meidani. Pi-vae: Physics-informed variational auto-encoder for stochastic differential equations. *Computer Methods in Applied Mechanics and Engineering*, 403:115664, 2023.

Appendix

This document provides supplementary materials for the paper titled *Towards Physically Interpretable World Models: Meaningful Weakly Supervised Representations for Visual Trajectory Prediction*. It includes additional figures, proofs, and experimental details that support the main text.

A Training and Prediction Algorithm

The training algorithm is shown in Algorithm 1. First, the training dataset, consisting of sequences of images, actions, and weak state labels, is divided into batches. For each batch, the observations are encoded using the encoder \mathcal{E} , and latent variables are sampled. The dynamics model ϕ predicts the latent variables for the next time step based on the current latent state and action. The decoder \mathcal{D} reconstructs the observed images, and the reconstruction loss is computed. The training process involves a single forward step to learn the parameters of the dynamics. The inference procedure is described in Algorithm 2, which demonstrates using an input sequence to predict over multiple horizons.

B Experiment Setup

We experiment on two well-known control tasks — lunar lander and cart pole [Brockman *et al.*, 2016] — to assess the proposed framework’s suitability for vision-based dynamical systems. In the cart pole, the task is to balance a pole on a moving cart by applying forces to the cart in one of two directions. This task has a four-dimensional state space (position, velocity, angle, and angular velocity) and a binary discrete action space (pull left or right), allowing only left or right movements. The lunar lander’s task is to guide a lander to a safe landing. This task has an eight-dimensional state space: horizontal and vertical positions, velocities, angle, angular velocity, and information about the lander’s contact with the ground. It also has a four-dimensional action space, allowing for finer control by activating the main engine and side thrusters. The lunar lander task is more complex than the cart pole, requiring precise control and handling of multiple variables, testing the model’s ability to capture complex relationships in both state and action spaces. There are 4 parameters of dynamics in a cart pole: the mass of the cart and pole, the length of the pole, and the force implemented on the cart. For the lunar lander, there are 2 parameters: the power of the main engine which controls the landing speed, and the power of the side engine which is responsible for adjusting the landing directions.

For each task, training, validation, and test data were collected from three different controllers that were trained with reinforcement learning (DQN) algorithm, ensuring diversity in the collected trajectories. For each task, $N = 60,000$, indicating the total number of trajectories collected, and $M = 50$, representing the number of time steps in each trajectory. The maximum of the prediction horizon is set to $k = 30$. 20,000 trajectories are collected for both validation and test datasets.

The encoder and decoder use basic convolutional and deconvolutional architectures, respectively. Baseline comparisons include VAE+LSTM and β -VAE+LSTM ($\beta=4$) models using the same loss functions, as well as a non-trainable,

true dynamical system for performance benchmarking. To test the effect of weak supervision, we applied interval constraints with lengths covering 2.5%, 5%, and 10% of the state space. These intervals were either centered around the true values or randomly shifted (noted as “shift” later in the result tables) so that the true values fell within the interval without necessarily being centered. This setup allowed us to examine how different levels of weak supervision, both with and without exact centering on the true values.

Another set of ablation experiments was conducted to assess how precise supervision using true state values impacts prediction accuracy and physical interpretability. In these experiments, the proposed model and baseline models (VAE&LSTM and β -VAE&LSTM) were trained using the loss function described in Alg 1, with true values as direct supervision signals. This setup provides ideal benchmarks for comparing the effectiveness of weak versus full supervision, allowing us to evaluate how much accuracy and physical alignment may be compromised under weak supervision conditions. These ablation experiments also allow us to investigate the effects of different loss function designs on model performance. While MSE enforces strict alignment with true values, weak supervision employs interval constraints, which allow some flexibility. This distinction reveals how loss functions shape model behavior.

All models are trained with a batch size of 32 and an initial learning rate of 0.001, using the Adam optimizer. Training was conducted for 200 epochs, with the learning rate set to decay when the loss plateaued.

All experiments were performed on an NVidia A100 GPU, which provided the computational power needed for handling high-dimensional inputs and complex dynamical simulations.

C Additional Experiments Results

Figure 3 presents the Mean Absolute Error (MAE) results for the Lunar Lander environment, showing the prediction errors for both vertical and horizontal positions. This highlights the differences in performance across models under various interval lengths and prediction horizons.

Figure 4 illustrates the MAE results for the Cart Pole environment, specifically for the cart’s position and the pole’s angle. These results demonstrate the prediction accuracy and model behavior under different weak supervision conditions.

Table 3 and Table 4 provide the corresponding numerical results for the Lunar Lander and Cart Pole experiments, respectively, detailing the MAE values for each model across varying interval lengths and prediction horizons.

D Dynamics of Lunar Lander and Cart Pole

Algorithm 3 and Algorithm 4 detail the dynamics of the Lunar Lander and Cart Pole environments, respectively.

In Algorithm 3, the dynamics for the Lunar Lander include the equations governing the horizontal and vertical positions, velocities, angle, angular velocity, and the effects of engine thrusts. These dynamics are used to simulate the lander’s motion and serve as the basis for evaluating the PIWM model’s ability to learn and predict the system’s behavior under varying levels of supervision.

In Algorithm 4, the dynamics for the Cart Pole environment capture the relationships between the cart’s position, velocity, pole angle, and angular velocity. These equations incorporate the applied forces and the resulting accelerations, demonstrating how the model learns the physical interactions within the system to generate accurate predictions.

Algorithm 1: Joint Learning of Physical Representation and Dynamics with Batch Input

Input: Training dataset V that contains sequences of images, actions, and weak state labels $(y_{1:M}, a_{1:M}, [x_{1:M}^{lo}, x_{1:M}^{up}])$, batch size B , controller h , weights λ_1, λ_2 and optimizer Adam()

Output: Well-trained PIWM model $(\mathcal{E}, \phi_\psi, \mathcal{D})$ with parameters θ

```

1 Initialize parameters  $\theta$  with random values;
2 for  $i \leftarrow 1$  to  $\text{len}(V)/B$  do
3   Sample a batch of  $B$  sequences from  $V$ ;
4   foreach sequence in batch do
5     for  $j \leftarrow 1$  to  $M - 1$  do
6        $(\mu_{z_j}, \sigma_{z_j}^2) = \mathcal{E}(y_j)$ ; // Encode
7       observations
8        $z_j \sim \mathcal{N}(\mu_{z_j}, \sigma_{z_j}^2)$ ; // Sample
9       latents
10       $z_{j+1} = \phi_\psi(z_j, a_j, \psi)$ ; // Predict
11      latents
12       $\hat{y}_{j+1} = \mathcal{D}(z_{j+1})$ ; // Reconstruct
13      image
14       $\mathcal{L}_0 = \frac{1}{D} \sum_{k=1}^D \|\hat{y}_{j+1} - y_{j+1}\|^2$ ;
15      // Reconstruction loss
16       $p \sim \mathcal{N}\left(\frac{x_{t-m:t}^{up} - x_{t-m:t}^{lo}}{2}, \left(\frac{x_{t-m:t}^{lo} + x_{t-m:t}^{up}}{6}\right)^2\right) =$ 
17       $\mathcal{N}(\mu_p, \sigma_p^2)$ ;
18       $q \sim \mathcal{N}(\mu_{z_j}, \sigma_{z_j}^2) = \mathcal{N}(\mu_q, \sigma_q^2)$ ;
19       $\mathcal{L}_1 =$ 
20       $\sum_{k=1}^d \left\| \frac{1}{2} \left( \frac{\sigma_p^2}{\sigma_q^2} + \frac{(\mu_q - \mu_p)^2}{\sigma_q^2} - 1 + \ln \frac{\sigma_q^2}{\sigma_p^2} \right) \right\|^2$ 
21      ; // KL divergence
22       $\mathcal{L}_2 = \lambda_2 \cdot \mathcal{L}_{\text{CE}}(h(\hat{y}_{j+1}), h(y_{j+1}))$ ;
23      // Action loss
24   Update parameters:
25    $\theta \leftarrow \text{Adam}(\theta, \nabla_\theta(\mathcal{L}_0 + \lambda_2 \mathcal{L}_1 + \lambda_2 \mathcal{L}_2))$ ;
26   ; // Update parameters over the
27   batch
28 return  $\theta$ 

```

Algorithm 2: PIWM Prediction Algorithm

Input: Observation y_t at any time t , predictor $\mathcal{P}_\theta = (\mathcal{E}, \phi_\psi, \mathcal{D})$, the length of state d and controller h

Output: Physical interpretable latent representations $z_{t:t+k}$, and predicted observation $\hat{y}_{t+1:t+k}$

```

1  $Z \leftarrow [], \hat{Y} \leftarrow []$ ; // Lists to store
2 predictions
3  $a \leftarrow a_t$ 
4  $(\mu_{z_t}, \sigma_{z_t}^2) = \mathcal{E}(y_t)$ ; // Encode images
5  $z_t \sim \mathcal{N}(\mu_{z_t}, \sigma_{z_t}^2)$ ; // Sample latents
6  $z'_t \leftarrow z_t[0:d]$ 
7 for  $i \leftarrow t$  to  $t+k$  do
8    $z'_{i+1} = \phi_\psi(z'_i, a, \psi)$ ; // Predict latents
9    $z_{i+1} \leftarrow [z'_{i+1}, z_i[d:d + \text{len}(z_i)]]$ 
10   $\hat{y}_{i+1} = \mathcal{D}(z_{i+1})$ ; // Reconstruct images
11   $\hat{Y}.\text{append}(\hat{y}_{i+1})$ 
12   $Z.\text{append}(z_{i+1})$ 
13   $a \leftarrow h(\hat{y}_{i+1})$ ; // Generate actions
14 return  $Z, \hat{Y}$ ;

```

Algorithm 3: Dynamics of Lunar Lander

Input: Current states $\mathbf{s} = [x, y, \dot{x}, \dot{y}, \theta, \dot{\theta}]$, actions \mathbf{a} (0: do nothing, 1: fire left, 2: fire main, 3: fire right)

Output: Updated states

```

1  $\mathbf{s}_{\text{new}} = [x_{\text{new}}, y_{\text{new}}, \dot{x}_{\text{new}}, \dot{y}_{\text{new}}, \theta_{\text{new}}, \dot{\theta}_{\text{new}}]$ 
2 // Unpack State Variables
3  $x \leftarrow \mathbf{s}[0], y \leftarrow \mathbf{s}[1], \dot{x} \leftarrow \mathbf{s}[2], \dot{y} \leftarrow \mathbf{s}[3]$ 
4  $\theta \leftarrow \mathbf{s}[4], \dot{\theta} \leftarrow \mathbf{s}[5]$ 
5 // Calculate Engine Direction and
6 Dispersion
7 tip  $\leftarrow [\sin(\theta), \cos(\theta)]$  side  $\leftarrow [-\cos(\theta), \sin(\theta)]$ 
8 // Process Actions
9 fire_main  $\leftarrow (\mathbf{a} == 2)$  fire_left  $\leftarrow (\mathbf{a} == 1)$ 
10 fire_right  $\leftarrow (\mathbf{a} == 3)$ 
11 // Compute Main Engine Thrust
12  $m_{\text{power}} \leftarrow \text{fire\_main}$ 
13  $\dot{x} \leftarrow \dot{x} - \text{tip}[0] \cdot \text{main\_power} \cdot m_{\text{power}}/\text{FPS}$ 
14  $\dot{y} \leftarrow \dot{y} + \text{tip}[1] \cdot \text{main\_power} \cdot m_{\text{power}}/\text{FPS}$ 
15 // Compute Side Engine Thrust
16  $s_{\text{power}} \leftarrow \text{fire\_left} + \text{fire\_right}$ 
17 direction  $\leftarrow \text{fire\_right} - \text{fire\_left}$ 
18  $\dot{x} \leftarrow \dot{x} + \text{side}[0] \cdot \text{side\_power} \cdot s_{\text{power}} \cdot \text{direction}/\text{FPS}$ 
19  $\dot{\theta} \leftarrow \dot{\theta} + \text{side}[1] \cdot s_{\text{power}} \cdot \text{direction}/\text{FPS}$ 
20 // Update Position and Angle
21  $x \leftarrow x + \dot{x}/\text{FPS}$   $y \leftarrow y + \dot{y}/\text{FPS}$   $\theta \leftarrow \theta + \dot{\theta}/\text{FPS}$ 
22 // Create Updated States
23  $\mathbf{s}_{\text{new}} \leftarrow [x, y, \dot{x}, \dot{y}, \theta, \dot{\theta}]$  return  $\mathbf{s}_{\text{new}}$ ;

```

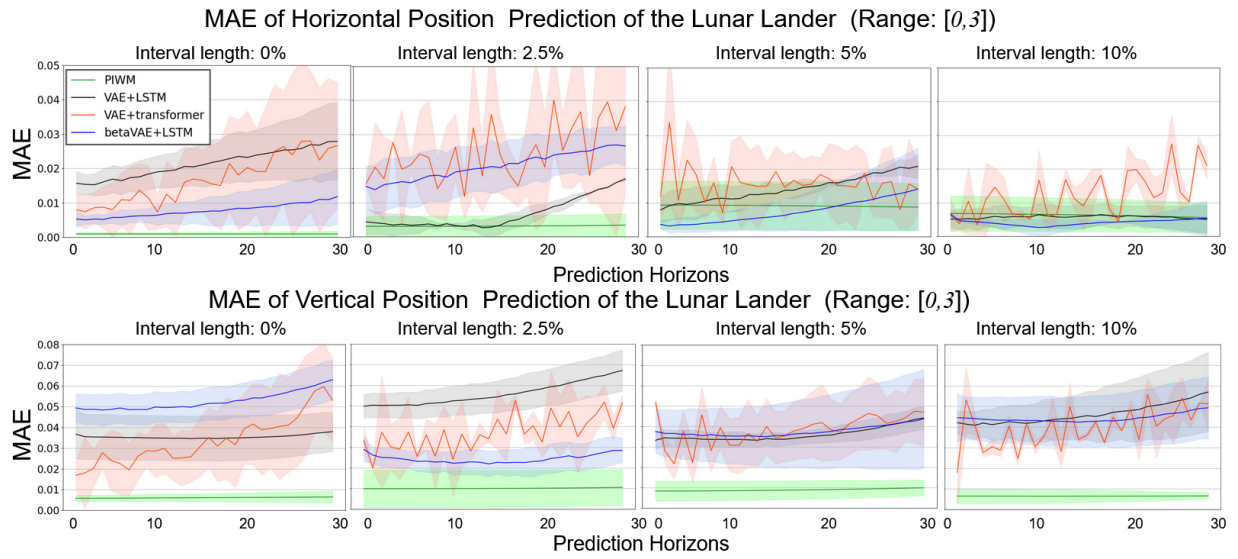


Figure 3: Results of the MAE of prediction, Lunar Lander.

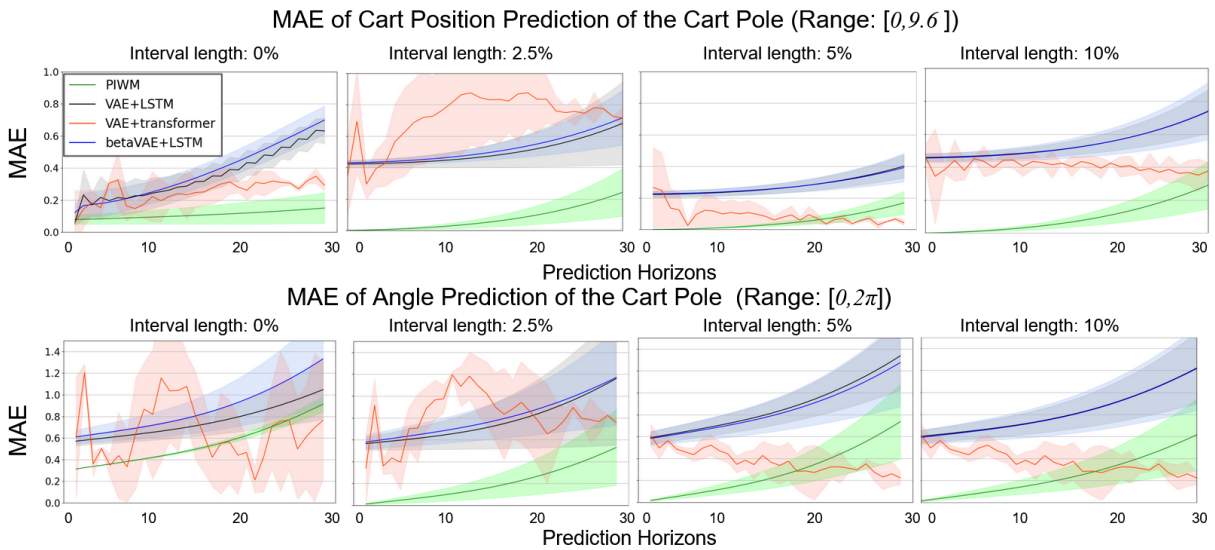


Figure 4: Results of the MAE of prediction, Cart Pole.

Table 3: State prediction performance for the *lunar lander*: the mean absolute error (MAE) for the lander’s horizontal and vertical position.

| Method | Interval length | Horizontal position error [-1.5, 1.5] | | | | Vertical position error [-1.5, 1.5] | | | |
|---------------------|-----------------|---------------------------------------|----------------------|----------------------|----------------------|-------------------------------------|----------------------|----------------------|----------------------|
| | | k=0 | k=10 | k=20 | k=30 | k=0 | k=10 | k=20 | k=30 |
| VAE & LSTM | 0 | 0.016 ± 0.003 | 0.019 ± 0.005 | 0.024 ± 0.007 | 0.028 ± 0.011 | 0.037 ± 0.012 | 0.035 ± 0.011 | 0.035 ± 0.011 | 0.038 ± 0.010 |
| VAE & Transformer | 0 | 0.008 ± 0.004 | 0.013 ± 0.009 | 0.019 ± 0.012 | 0.027 ± 0.018 | 0.017 ± 0.007 | 0.030 ± 0.012 | 0.042 ± 0.020 | 0.053 ± 0.020 |
| β -VAE & LSTM | 0 | 0.005 ± 0.002 | 0.007 ± 0.003 | 0.009 ± 0.005 | 0.012 ± 0.008 | 0.049 ± 0.007 | 0.050 ± 0.007 | 0.054 ± 0.009 | 0.063 ± 0.010 |
| PIWM | 0 | 0.001 ± 0.000 | 0.001 ± 0.000 | 0.001 ± 0.001 | 0.001 ± 0.001 | 0.006 ± 0.002 | 0.006 ± 0.002 | 0.006 ± 0.002 | 0.006 ± 0.003 |
| VAE & LSTM | 2.5% | 0.004 ± 0.004 | 0.003 ± 0.001 | 0.008 ± 0.002 | 0.017 ± 0.001 | 0.050 ± 0.006 | 0.052 ± 0.007 | 0.058 ± 0.009 | 0.067 ± 0.010 |
| VAE & Transformer | 2.5% | 0.016 ± 0.001 | 0.026 ± 0.010 | 0.020 ± 0.016 | 0.038 ± 0.026 | 0.033 ± 0.007 | 0.024 ± 0.018 | 0.033 ± 0.007 | 0.051 ± 0.004 |
| β -VAE & LSTM | 2.5% | 0.015 ± 0.006 | 0.019 ± 0.008 | 0.023 ± 0.007 | 0.027 ± 0.006 | 0.029 ± 0.006 | 0.022 ± 0.006 | 0.023 ± 0.007 | 0.028 ± 0.006 |
| PIWM | 2.5% | 0.003 ± 0.003 | 0.003 ± 0.003 | 0.003 ± 0.003 | 0.003 ± 0.003 | 0.010 ± 0.009 | 0.010 ± 0.009 | 0.010 ± 0.009 | 0.011 ± 0.009 |
| VAE & LSTM | 5% | 0.008 ± 0.004 | 0.012 ± 0.003 | 0.016 ± 0.001 | 0.021 ± 0.004 | 0.033 ± 0.004 | 0.033 ± 0.003 | 0.037 ± 0.004 | 0.044 ± 0.006 |
| VAE & Transformer | 5% | 0.012 ± 0.006 | 0.015 ± 0.010 | 0.015 ± 0.012 | 0.014 ± 0.008 | 0.052 ± 0.002 | 0.037 ± 0.017 | 0.037 ± 0.014 | 0.047 ± 0.016 |
| β -VAE & LSTM | 5% | 0.004 ± 0.001 | 0.005 ± 0.003 | 0.009 ± 0.007 | 0.014 ± 0.012 | 0.038 ± 0.011 | 0.036 ± 0.014 | 0.038 ± 0.019 | 0.044 ± 0.024 |
| PIWM | 5% | 0.009 ± 0.007 | 0.009 ± 0.007 | 0.009 ± 0.007 | 0.009 ± 0.007 | 0.008 ± 0.005 | 0.009 ± 0.005 | 0.009 ± 0.004 | 0.010 ± 0.004 |
| VAE & LSTM | 10% | 0.005 ± 0.003 | 0.006 ± 0.003 | 0.006 ± 0.003 | 0.005 ± 0.004 | 0.042 ± 0.006 | 0.043 ± 0.010 | 0.048 ± 0.015 | 0.057 ± 0.019 |
| VAE & Transformer | 10% | 0.006 ± 0.005 | 0.017 ± 0.009 | 0.020 ± 0.007 | 0.021 ± 0.004 | 0.018 ± 0.016 | 0.035 ± 0.001 | 0.049 ± 0.004 | 0.051 ± 0.012 |
| β -VAE & LSTM | 10% | 0.006 ± 0.001 | 0.003 ± 0.002 | 0.004 ± 0.000 | 0.005 ± 0.005 | 0.045 ± 0.012 | 0.043 ± 0.012 | 0.044 ± 0.013 | 0.049 ± 0.015 |
| PIWM | 10% | 0.007 ± 0.005 | 0.007 ± 0.005 | 0.006 ± 0.005 | 0.006 ± 0.004 | 0.006 ± 0.004 | 0.006 ± 0.003 | 0.006 ± 0.003 | 0.007 ± 0.002 |

Table 4: State prediction performance for the *cart pole*: the mean absolute error (MAE) for the cart’s position and the pole’s angle.

| Method | Interval length | Horizontal position error [0, 9.6] | | | | Vertical position error [0, 2 π] | | | |
|---------------------|-----------------|------------------------------------|----------------------|----------------------|----------------------|---------------------------------------|----------------------|----------------------|----------------------|
| | | k=0 | k=10 | k=20 | k=30 | k=0 | k=10 | k=20 | k=30 |
| VAE & LSTM | 0 | 0.056 ± 0.056 | 0.252 ± 0.252 | 0.434 ± 0.434 | 0.632 ± 0.632 | 0.571 ± 0.571 | 0.664 ± 0.664 | 0.814 ± 0.814 | 1.047 ± 1.047 |
| VAE & Transformer | 0 | 0.058 ± 0.020 | 0.196 ± 0.133 | 0.261 ± 0.060 | 0.292 ± 0.031 | 0.605 ± 0.562 | 1.156 ± 0.779 | 0.467 ± 0.120 | 0.763 ± 0.546 |
| β -VAE & LSTM | 0 | 0.122 ± 0.122 | 0.266 ± 0.266 | 0.467 ± 0.467 | 0.699 ± 0.699 | 0.610 ± 0.610 | 0.733 ± 0.733 | 0.959 ± 0.959 | 1.332 ± 1.332 |
| PIWM | 0 | 0.079 ± 0.029 | 0.096 ± 0.045 | 0.119 ± 0.069 | 0.151 ± 0.095 | 0.314 ± 0.000 | 0.434 ± 0.007 | 0.622 ± 0.029 | 0.914 ± 0.072 |
| VAE & LSTM | 2.5% | 0.211 ± 0.012 | 0.222 ± 0.023 | 0.260 ± 0.057 | 0.341 ± 0.132 | 0.565 ± 0.060 | 0.655 ± 0.142 | 0.840 ± 0.315 | 1.160 ± 0.610 |
| VAE & Transformer | 2.5% | 0.172 ± 0.120 | 0.383 ± 0.163 | 0.418 ± 0.108 | 0.358 ± 0.034 | 0.341 ± 0.316 | 1.194 ± 0.033 | 0.768 ± 0.416 | 0.758 ± 0.028 |
| β -VAE & LSTM | 2.5% | 0.215 ± 0.007 | 0.231 ± 0.015 | 0.275 ± 0.038 | 0.358 ± 0.087 | 0.579 ± 0.065 | 0.696 ± 0.123 | 0.883 ± 0.235 | 1.171 ± 0.438 |
| PIWM | 2.5% | 0.008 ± 0.000 | 0.012 ± 0.008 | 0.049 ± 0.030 | 0.121 ± 0.076 | 0.012 ± 0.007 | 0.106 ± 0.064 | 0.269 ± 0.168 | 0.529 ± 0.347 |
| VAE & LSTM | 5% | 0.222 ± 0.022 | 0.241 ± 0.026 | 0.296 ± 0.041 | 0.401 ± 0.074 | 0.590 ± 0.057 | 0.736 ± 0.092 | 0.971 ± 0.168 | 1.337 ± 0.315 |
| VAE & Transformer | 5% | 0.266 ± 0.256 | 0.100 ± 0.074 | 0.035 ± 0.007 | 0.042 ± 0.015 | 0.611 ± 0.101 | 0.347 ± 0.078 | 0.301 ± 0.186 | 0.223 ± 0.060 |
| β -VAE & LSTM | 5% | 0.226 ± 0.018 | 0.243 ± 0.025 | 0.295 ± 0.046 | 0.392 ± 0.091 | 0.582 ± 0.062 | 0.718 ± 0.116 | 0.935 ± 0.217 | 1.275 ± 0.403 |
| PIWM | 5% | 0.010 ± 0.000 | 0.017 ± 0.007 | 0.068 ± 0.029 | 0.168 ± 0.074 | 0.016 ± 0.006 | 0.147 ± 0.060 | 0.373 ± 0.163 | 0.736 ± 0.343 |
| VAE & LSTM | 10% | 0.229 ± 0.012 | 0.242 ± 0.016 | 0.284 ± 0.031 | 0.369 ± 0.066 | 0.601 ± 0.059 | 0.704 ± 0.094 | 0.898 ± 0.174 | 1.221 ± 0.324 |
| VAE & Transformer | 10% | 0.231 ± 0.038 | 0.203 ± 0.031 | 0.202 ± 0.031 | 0.188 ± 0.027 | 0.611 ± 0.101 | 0.347 ± 0.078 | 0.301 ± 0.186 | 0.223 ± 0.060 |
| β -VAE & LSTM | 10% | 0.228 ± 0.014 | 0.241 ± 0.021 | 0.284 ± 0.043 | 0.370 ± 0.087 | 0.592 ± 0.062 | 0.699 ± 0.118 | 0.894 ± 0.217 | 1.216 ± 0.380 |
| PIWM | 10% | 0.013 ± 0.000 | 0.016 ± 0.007 | 0.061 ± 0.029 | 0.145 ± 0.072 | 0.015 ± 0.007 | 0.135 ± 0.063 | 0.323 ± 0.160 | 0.615 ± 0.325 |

Algorithm 4: Dynamics of Cart Pole

Input: Current state $z = [x, \dot{x}, \theta, \dot{\theta}]$, action a
Output: Updated state $z_{\text{new}} = [x_{\text{new}}, \dot{x}_{\text{new}}, \theta_{\text{new}}, \dot{\theta}_{\text{new}}]$
// Extract State Variables
1 $x, \dot{x}, \theta, \dot{\theta} \leftarrow z[:, 0], z[:, 1], z[:, 2], z[:, 3]$
// Convert Action to Force
2 $F \leftarrow \text{force_mag} \times (2 \cdot a - 1)$
// Compute Trigonometric Values
3 $\cos(\theta) \leftarrow \text{costheta}, \sin(\theta) \leftarrow \text{sintheta}$
// Compute Intermediate Variable
4 $\text{temp} \leftarrow \frac{F + m_p \cdot l \cdot \dot{\theta}^2 \cdot \sin(\theta)}{m_p + m_c}$
// Calculate Angular Acceleration
5 $\ddot{\theta} \leftarrow \frac{g \cdot \sin(\theta) - \cos(\theta) \cdot \text{temp}}{l \cdot \left(\frac{4}{3} - \frac{m_p \cdot \cos^2(\theta)}{m_p + m_c} \right)}$
// Calculate Linear Acceleration
6 $\ddot{x} \leftarrow \text{temp} - \frac{m_p \cdot l \cdot \ddot{\theta} \cdot \cos(\theta)}{m_p + m_c}$
// Update State Variables
7 $x_{\text{new}} \leftarrow x + \tau \cdot \dot{x} \quad \dot{x}_{\text{new}} \leftarrow \dot{x} + \tau \cdot \ddot{x} \quad \theta_{\text{new}} \leftarrow \theta + \tau \cdot \dot{\theta}$
 $\dot{\theta}_{\text{new}} \leftarrow \dot{\theta} + \tau \cdot \ddot{\theta}$
// Return Updated State
8 $z_{\text{new}} \leftarrow [x_{\text{new}}, \dot{x}_{\text{new}}, \theta_{\text{new}}, \dot{\theta}_{\text{new}}]$ **return** z_{new} ;